

Article

Thermodynamic Analysis of Three Compressed Air Energy Storage Systems: Conventional, Adiabatic, and Hydrogen-Fueled

Hossein Safaei and Michael J. Aziz *

Harvard John A. Paulson School of Engineering and Applied Sciences, Pierce Hall, 29 Oxford Street, Cambridge, MA 02138, USA; Hossein.Safaei@gmail.com

* Correspondence: maziz@harvard.edu; Tel.: +1-617-495-9884

Received: 10 May 2017; Accepted: 27 June 2017; Published: 18 July 2017

Abstract: We present analyses of three families of compressed air energy storage (CAES) systems: conventional CAES, in which the heat released during air compression is not stored and natural gas is combusted to provide heat during discharge; adiabatic CAES, in which the compression heat is stored; and CAES in which the compression heat is used to assist water electrolysis for hydrogen storage. The latter two methods involve no fossil fuel combustion. We modeled both a low-temperature and a high-temperature electrolysis process for hydrogen production. Adiabatic CAES (A-CAES) with physical storage of heat is the most efficient option with an exergy efficiency of 69.5% for energy storage. The exergy efficiency of the conventional CAES system is estimated to be 54.3%. Both high-temperature and low-temperature electrolysis CAES systems result in similar exergy efficiencies (35.6% and 34.2%), partly due to low efficiency of the electrolyzer cell. CAES with high-temperature electrolysis has the highest energy storage density (7.9 kWh per m³ of air storage volume), followed by A-CAES (5.2 kWh/m³). Conventional CAES and CAES with low-temperature electrolysis have similar energy densities of 3.1 kWh/m³.

Keywords: compressed air energy storage (CAES); adiabatic CAES; high temperature electrolysis; hydrogen storage; thermodynamics

1. Introduction

Large penetrations of wind and solar energies challenge the reliability of the electricity grid, due to their intermittency and uncertainty. Storage technologies are being developed to tackle this challenge. Compressed air energy storage (CAES) is a relatively mature technology with currently more attractive economics compared to other bulk energy storage systems capable of delivering tens of megawatts over several hours, such as pumped hydroelectric [1–3]. CAES stores electrical energy as the exergy of compressed air. Figure 1 is a simplified schematic of a CAES plant. Electricity is supplied by the grid to run the air compressors and charge the storage system. Waste heat is released during the compression phase. Air is stored for later use—often in an underground cavern. During the discharge phase, compressed air is combusted with a fuel, and expanded in a turbine (expander) to regenerate electricity. Currently, there are two commercial CAES plants in operation: Huntorf in Germany (since 1978) and McIntosh in USA (since 1991) [4]. Moreover, there are some smaller projects in operations or in construction and planning phases, most notably General Compression's 2 MW, 300 MWh project in Texas, USA and SustainX's 1.5 MW, 1 MWh project in New Hampshire, USA [5].

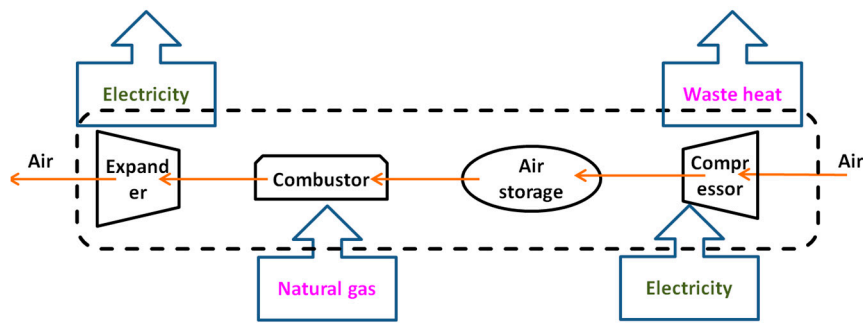


Figure 1. Schematic of a generic conventional compressed air energy storage (CAES) system.

The prospects for the conventional CAES technology are poor in low-carbon grids [2,6–8]. Fossil fuel (typically natural gas) combustion is needed to provide heat to prevent freezing of the moisture present in the expanding air [9]. Fuel combustion also boosts the work output in comparison to solely harnessing the energy stored in the compressed air.

We develop analytical models to assess the thermodynamics of two strategies to make CAES greenhouse gas (GHG) emissions-free. Both utilize the temperature increase from the air compression process to eliminate the need for gas combustion. This heat is generated during the charging phase. Because of its low temperature and correspondingly low exergy, the compression heat is rejected to the ambient environment in the conventional CAES setup. This heat could, in principle, be stored to heat the expanding air provided that the temperature of this stored heat is high enough. The primary method to achieve such high temperatures is to increase the operating pressure of the compressors and to eliminate intercooling between compression stages (i.e., adiabatic compression). This, however, poses practical challenges due to high operating pressures and temperatures of the compressors (e.g., metallurgical limits on compressor blades).

Physical storage of the compression heat is the core of the Adiabatic CAES (A-CAES) concept—the first carbon-free CAES system we investigate. Chemical storage of the compression heat in the form of hydrogen, and combustion of hydrogen instead of natural gas during the discharge phase is the second strategy we analyzed. Hydrogen can be produced via electrolysis of steam at high temperatures (HTE) or water at low (ambient) temperatures (LTE). The HTE concept benefits from the lower electricity demand of the electrolysis process at higher temperatures. Utilizing the high-temperature heat of compression lowers the electricity demand of hydrogen production in the CAES-HTE system. This saving is achieved at the expense of higher electricity demand of the air compressor which, in CAES-HTE, operates at higher pressures with limited or no cooling. The CAES-LTE concept is comparable to the conventional CAES system (diabatic compression with the use of coolers between compressor stages). However, hydrogen is produced onsite with a low-temperature electrolyzer.

Electrolysis of steam (HTE) instead of water (LTE) requires more thermal but less electrical energy. Figure 2 illustrates the theoretical energy requirements as functions of the electrolysis reaction temperature (see Appendix A for details). In a high-temperature electrolyzer, steam is disassociated in the cathode to produce hydrogen and O^{2-} , while O^{2-} is oxidized in the anode to produce oxygen. The theoretical total energy demand of the electrolysis process (change in enthalpy, ΔH) equals the electricity demand (reversible work, i.e., change in the Gibbs free energy, ΔG) plus the heat demand of the reaction (change in entropy multiplied by the reaction temperature, $\Delta S \times T$) from a source of at least as high a temperature as the reaction temperature. While the total energy demand (enthalpy change) of electrolyzing steam increases at higher temperatures, its electricity demand decreases. The savings in electricity consumption of the electrolyzer come at the expense of its higher heat load. Therefore, electrolysis of steam instead of water could be particularly attractive when electricity supply is constrained and high-temperature heat is abundant. Note that the actual electricity demand of

the electrolyzers will be higher than the theoretical value (ΔG) because the electrolyzer cell efficiency is less than 100%.

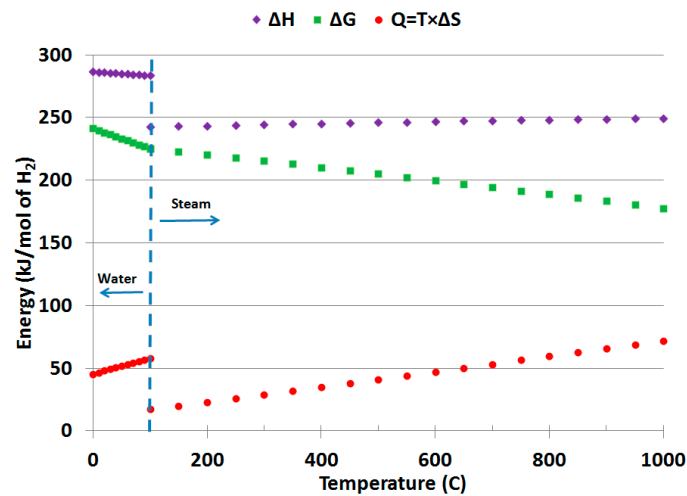


Figure 2. Theoretical energy demand for electrolysis as a function of the reaction temperature.

Existing literature has studied the thermodynamics of conventional CAES [10–15], A-CAES [16–22], and combustion of hydrogen instead of natural gas to fuel conventional CAES [23]. Moreover, alternative advanced CAES designs have also been studied such as isothermal CAES, CAES paired with cogeneration of heat and power, CAES with humidification, and trigeneration CAES systems [24–29].

With this paper, we introduce the concepts of CAES-HTE and CAES-LTE, and provide a comparative thermodynamic analysis of these approaches against A-CAES and conventional CAES. We also assess the sensitivity of our results to two key design parameters: the storage pressure of compressed air and the maximum discharge temperature of the high-pressure compressor. CAES-HTE can potentially be an alternative to A-CAES as a zero-carbon energy storage system that makes use of the otherwise wasted heat of compression. A-CAES stores it as high-temperature thermal energy whereas CAES-HTE stores it as chemical energy. This paper explores whether the use of the compression heat at sufficiently high temperatures could reduce the electricity demand of hydrogen production enough to make the efficiency of CAES-HTE competitive with A-CAES. CAES-LTE is analyzed to provide the most direct baseline for CAES-HTE.

Based on our analysis, A-CAES scored the highest storage efficiency (69.6%) followed by conventional CAES (54.3%), CAES-HTE (35.6%, assuming an electrolyzer efficiency of 50%), and CAES-LTE (34.2%, assuming an electrolyzer efficiency of 50%). CAES-HTE has the highest energy storage density (7.9 kWh per m^3 of storage volume) compared with A-CAES (5.2 kWh/ m^3). Conventional CAES and CAES-LTE have similar energy intensities (3.1 kWh/ m^3). The conventional CAES system modeled here uses natural gas at a rate of 3.97 GJ per MWh of gross (total) electricity generated. This corresponds to 15.27 GJ per MWh of net or incremental electricity (difference between electricity released and stored) delivered by the plant. Other technical figures of merit are introduced and evaluated as well.

2. Materials and Methods

We use an analytical model to compare the thermodynamics of the conventional CAES, A-CAES, CAES-HTE, and CAES-LTE systems. Our general strategy is applying the First and Second Laws of thermodynamics to the individual system components and modeling air as an ideal gas with temperature-independent specific heat values. We quantify the mass, energy, and exergy flows into and out of the storage facility. The schematics of the modeled conventional CAES, A-CAES, CAES-HTE and CAES-LTE systems are illustrated in Figures 3–6.

We also assess the sensitivity of our results to two key design parameters: the storage pressure of compressed air and the maximum discharge temperature of the high-pressure compressor.

The modeled compressed air storage systems use both electrical energy (to compress air and possibly to generate hydrogen) and heating energy provided by natural gas (only conventional CAES). We use three metrics to compare their energy use: heat rate, work ratio, and roundtrip exergy efficiency (storage efficiency). The heat rate is defined as the external heating fuel (natural gas here) consumed per unit of gross (total) electricity generated by the storage plant (GJ/MWh, on a lower heating value basis, LHV). The heat rate of A-CAES, CAES-HTE, and CAES-LTE is zero as they do not use an external fuel (i.e., natural gas). We also report the heat rate based on the net (incremental) electricity delivered by the storage plant. This metric assists in comparing conventional CAES with conventional gas turbines to manage intermittency of wind and solar in low-carbon grids.

The work ratio quantifies the amount of electrical energy consumed by the compressor (and also the electrolyzer, when applicable) per unit of gross electrical energy generated by the expander. The roundtrip exergy efficiency is the ratio of the exergy delivered (i.e., turbine work) to the exergy provided to the storage plant. The input exergy is the summation of the compression work, the LHV exergy of natural gas (conventional CAES), and the electricity consumed by the electrolyzer (CAES-HTE and CAES-LTE).

One of the critiques of using compressed air to store electricity at scale is its low exergy density. Here, we define exergy density of the storage facility as the ratio of the delivered exergy (i.e., expansion work) to the volume of the air storage cavern. Exergy density is especially important when the storage medium is scarce.

We define the emissions intensity as the ratio of the GHG emissions from natural gas consumption to the gross electricity supply by the storage plant (i.e., total electricity delivered). This variable is zero for all systems studied except conventional CAES—the only configuration in which a fossil fuel is burned. As we do for the heat rate, we express the emissions intensity of conventional CAES based on both the gross and the net electricity delivered.

This section summarizes our general modeling assumptions and simplifications. See Appendix A and nomenclature for the full thermodynamic analysis and the list of symbols.

We model one complete charge and discharge cycle at full load of the compressor and expander (i.e., no part-load operations). We treat air as an ideal gas with temperature-independent specific heat. We ignore the fuel mass and treat the mixture of air and fuel as pure air. Equations (1)–(5) show the general ideal gas formulae we use. The ambient environment (subscript 0) is set at the standard ambient temperature and pressure of 25 °C and 101 kPa. This condition is the reference state for calculating the internal energy, enthalpy, entropy, and exergy throughout our analysis.

$$m = \frac{P V}{R T} \quad \text{mass of the air present in cavern} \quad (1)$$

$$h = (T - T_0)C_p \quad \text{specific enthalpy of air} \quad (2)$$

$$u = (C_v T) - (C_p T_0) \quad \text{specific internal energy of air} \quad (3)$$

$$s = C_p \ln\left(\frac{T}{T_0}\right) - R \ln\left(\frac{P}{P_0}\right) \quad \text{specific entropy of air} \quad (4)$$

$$\psi = (h - h_0) - (s - s_0)T_0 \quad \text{specific stream exergy of air} \quad (5)$$

The air storage cavern has a fixed volume. Its pressure varies between a minimum (P_{em}) and a maximum (P_{fl}) during the charge and discharge processes. In order to maintain its mechanical integrity and to ensure high-enough flow rates for the discharging air, the cavern is not fully discharged in practice. The air mass remaining in the storage at the end of the discharge phase (when all the “working air” has been withdrawn) is called the “cushion air”. We model the cavern as adiabatic. Raju et al. [10], Steta [20], and Xia et al. [30] studied heat transfer between the stored air and the cavern wall, which is beyond the scope of our work. The rate of heat transfer depends on several factors

such as residence time of air in the cavern and its temperature, rock properties, cavern size and shape. Raju et al. estimated the rate of heat loss at the Huntorf CAES plant in the order of few percent of the compressor power.

The coolers (heat exchangers) following each compression stage are assigned a fixed approach temperature, T_{ac} . This is defined as the difference between the temperature of the cooling fluid (e.g., water) entering the cooler ($T_{in,coolant}^{CL}$, set at T_0) and that of the cooled compressed air leaving the compressor cooler ($T_{out,air}^{CL}$). This implies the inlet temperature of the cavern and the output of all the compressor coolers are fixed and equal to $T_{ac} + T_0$ (see Equation (6)).

$$T_{in}^{CN} = T_{out,air}^{CL} = T_{ac} + T_0 \quad \text{inlet temperature of cavern and discharge of compressor coolers} \quad (6)$$

The discharge temperature of the combustion chambers (T_{out}^{cc}) is maintained at a fixed value. The expander has two stages. The high-pressure (HP) and low-pressure (LP) stages, which have equal but variable expansion ratios (XR) and determined according to the instantaneous pressure of the cavern (Equation (7)).

$$XR_{HP} = XR_{LP} = \sqrt{\frac{P_0}{P_{CN}}} = \sqrt{XR} \quad \text{instantaneous expansion ratio} \quad (7)$$

The temperature of the air stream leaving the storage plant during the discharge process (T_{et}) is constrained to be fixed and constant. Following Osterle [13], an imaginary final heat exchanger (FHX) is placed at the exhaust of the storage plant to account for the exergy loss by the exhaust stream to the ambient environment. This heat exchanger cools down the expanded air from T_{et} to the ambient temperature.

Heat flows (Q) are reckoned to be positive if they enter the system (e.g., heat added in the combustor). Work done by the system on the surroundings has a positive sign (e.g., expansion work).

As shown in the Appendix A, the First and Second Laws of thermodynamics are applied to each system component to quantify the work, heat, and exergy fluxes during the charge and discharge processes. Once these are determined, the roundtrip exergy efficiency ($\eta_{storage}$), work ratio (WR), heat rate (HR), emissions intensity (GI_{plant}), and exergy density (ρ) of the storage plant are calculated by applying Equations (8)–(12).

$$\eta_{storage} = \frac{W_{TB}}{-W_{CM} + X_{NG} - W_{electrolysis}} \quad (8)$$

$$WR = \frac{-W_{CM} - W_{electrolysis}}{W_{TB}} \quad (9)$$

$$HR = \left(\frac{m_{NG} LHV_{NG}}{W_{TB}} \right) \left(\frac{3.6 \text{ GJ}}{\text{MWh}} \right) \quad (10)$$

$$GI_{plant} = (HR)(GI_{NG}) \quad (11)$$

$$\rho = \frac{W_{TB}}{V} \quad (12)$$

2.1. Modeling Conventional CAES

In the conventional CAES system we modeled (Figure 3), air is compressed in a three-stage compressor (CM) and then stored in the cavern (CN). Each compression stage is followed by a cooler (CL) to reduce the compression work of the succeeding stage and to reduce the volumetric requirement of air storage by increasing the density of the stored air. The compression heat is released to the ambient environment.

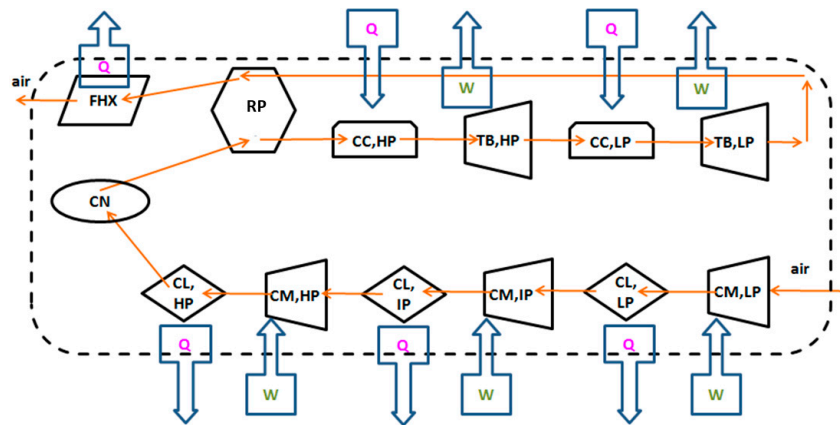


Figure 3. Schematic of the conventional CAES system. The compression train (CM) is composed of three stages: low-, intermediate-, and high-pressure (LP, IP, and HP). The expansion train (TB) is made of high- and low-pressure stages (HP and LP). “Q” and “W” represent heat and work interactions between the system and the surroundings. The air leaving the cavern is preheated in the recuperator by the hot air leaving the low pressure turbine (internal heat transfer). “0” indicates ambient condition. CL, CN, CC, RP, and FHX stand for the cooler, cavern, combustor, recuperator, and final exhaust heat exchanger.

During the discharge phase, air is first preheated in a recuperator (RP). It is then combusted with natural gas (NG) to generate work in the expanders (turbines, TB). We modeled a two-stage expander. In the recuperator, the exhaust of the low-pressure turbine preheats the air leaving the cavern and entering the high-pressure combustor to reduce the fuel demand.

The compressor has three stages: low (LP), intermediate (IP), and high pressure (HP). All stages have variable but equal compression ratios throughout the charging process. The compression ratios (CR) vary according to the instantaneous pressure of the cavern.

2.2. Modeling A-CAES

Figure 4 illustrates the A-CAES system we analyzed. The compression heat is stored in two thermal energy storage systems (TS1 and TS2). Coolers between compression stages are eliminated in A-CAES to increase the discharge temperature of the compressors. We therefore, model a two-stage (LP and HP) compressor. Only one cooler (heat exchanger, between the TS2 discharge and the cavern inlet) exists and cools the compressed air prior to storage.

The expansion train of A-CAES is made up of two stages (HP and LP). The withdrawn compressed air is heated in TS1 and TS2 before expanding and generating electricity (combustors are eliminated). No recuperator is considered. This is owing to the low discharge temperature of the LP expander. The discharge stream is cooled to the ambient temperature in the final exhaust heat exchanger (FHX). TS1 absorbs heat from the air leaving the low-pressure compressor and provides heat to the compressed air entering the high-pressure expander. TS2 interacts with the high-pressure compressor and the low-pressure expander. Refer to Appendix A for more details.

Similar to the analysis of conventional CAES, the temperature of the air entering the cavern is set as constant. The intake temperatures of the expanders (i.e., exhaust of TS1 and TS2) are constrained to be constant. However, their values are dictated by the amount of heat stored during the charging phase. Note that the inlet temperatures of the expanders in the conventional CAES system were constant as well, but their values were a preset design parameter, satisfied by variable combustion rates. The TS1 and TS2 units are modeled as isobaric and adiabatic.

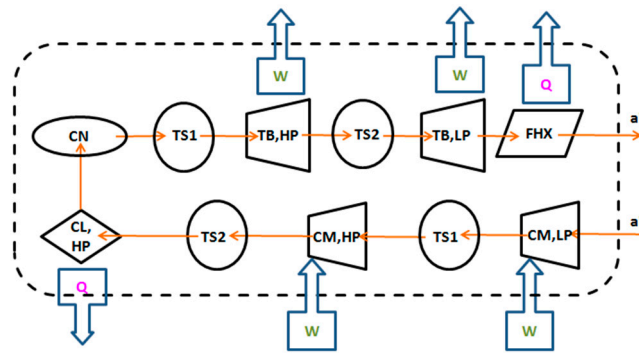


Figure 4. Schematic of the A-CAES system. All of the low pressure (LP) and a portion of the high pressure (HP) compression heat are stored in two thermal storage facilities (TS1 and TS2). The same heat storage units release the heat to the withdrawn compressed air prior to expansion during the discharge phase. “Q” and “W” represent heat and work interactions between the system and the surroundings.

The maximum exit temperature of the high-pressure compressor is a preset parameter, which will be varied in the sensitivity analysis section. Our rationale for this design constraint is the following. The exit temperature of the compressor is a key parameter for determining the exergy supplied to and stored in thermal storage. This consequently impacts the temperature of the air entering the expanders. Moreover, there are technical constraints such as the stress on and the fatigue of compressor blades driven by the maximum exit temperature of the compressor [31,32].

Once a full charge and discharge cycle is modeled, the overall performance of A-CAES are characterized with Equations (8)–(12). The heat rate and GHG emissions intensity of A-CAES are zero as no fuel is consumed.

2.3. Modeling CAES-HTE and CAES-LTE

As illustrated in Figure 5, the compressor of CAES-HTE is made up of two stages similar to A-CAES to increase the temperature of the compression heat stored, in contrast to our CAES-LTE and conventional CAES models with three stage compressors. A heat exchanger cools the exhaust stream of the LP compressor to a constant temperature before entering the HP compressor. The maximum discharge temperature of the HP compressor is a design parameter and is preset, similar to the A-CAES model. Whereas using a one stage compressor could generate higher temperature heat, the operating temperature of the compressor would be in excess of 1000 °C, compared to the 500–700 °C range considered in the literature for practical reasons (e.g., mechanical integrity of compressor blades) [31,32]. The heat absorbed from the exhaust stream of the HP compressor is used to make steam, to heat up the steam to the constant temperature of the electrolyzer, and to provide the heating energy required for the electrolysis process. A heat exchanger follows the electrolyzer to further cool the compressed air to a fixed temperature before entering the cavern. The generated hydrogen is stored to burn and heat the air during the discharge phase. We choose not to consider any physical storage of heat, similar to conventional CAES and in contrast to A-CAES. This is due to the relatively low temperature of air upon giving its heat to the HTE system. The discharge phase of CAES-HTE is identical to that of conventional CAES with the distinction that hydrogen (produced during charging), instead of natural gas, fuels the combustors.

The simulated CAES-LTE system (Figure 6) has a similar configuration as the CAES-HTE system, with the difference that a low-temperature electrolyzer (LTE) is used instead of a HTE. Moreover, a three-stage compression train is used, similar to conventional CAES. This is because there is no need to produce high-temperature heat. Increasing the number of compression stages in CAES-LTE reduces the compression work compared to CAES-HTE.

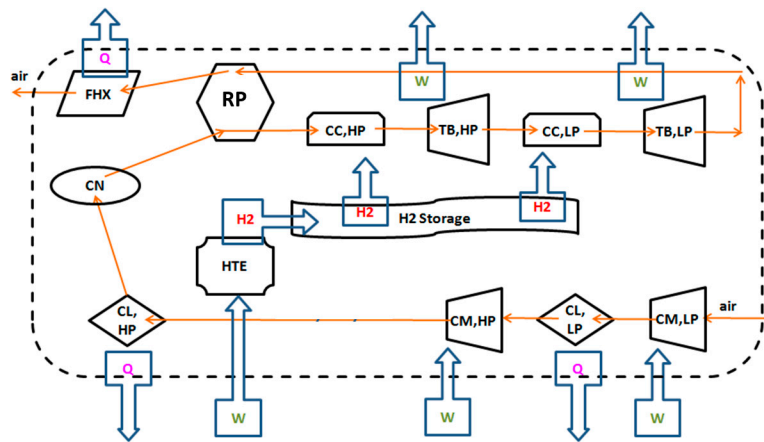


Figure 5. Schematic of the CAES-HTE system simulated. HTE stands for high temperature electrolyzer. “Q” and “W” represent heat and work interactions between the system and the surroundings. The air leaving the cavern is preheated in the recuperator by the hot air leaving the low pressure turbine (internal heat transfer). The air leaving the high pressure compressor provides the heat demand of the HTE (internal heat transfer).

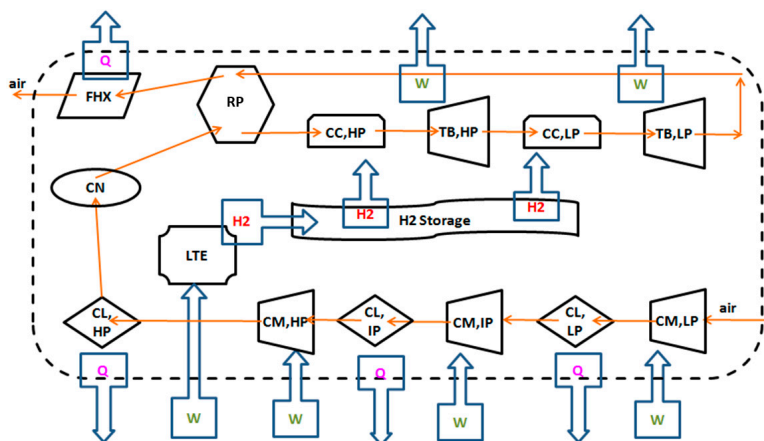


Figure 6. Schematic of the CAES-LTE system simulated. LTE stands for low temperature electrolyzer. “Q” and “W” represent heat and work interactions between the system and the surroundings. The air leaving the cavern is preheated in the recuperator by the hot air leaving the low pressure turbine (internal heat transfer).

Analysis of CAES-LTE is similar to that of CAES-HTE. The difference is that there is no explicit constraint on the maximum temperature of the air leaving the HP compressor. This is because the utilization of a three stage compressor and coolers results in temperature below the metallurgical limit of the turbines blades, similar to the conventional CAES design.

The heat rate and GHG emissions intensity of both CAES-HTE and CAES-LTE are zero because they burn hydrogen rather than natural gas. The storage efficiency and work ratio of the systems are quantified by Equations (8) and (9). CAES-HTE and CAES-LTE have higher work ratios compared to conventional CAES because of the work load of the electrolyzer.

3. Results

This section provides a series of numerical examples based on the analytical models developed in Section 2 and in Appendix A. The main question being addressed is whether the chemical storage of the high-temperature heat of compression as hydrogen (CAES-HTE) is thermodynamically superior

to the physical storage of the heat (A-CAES). The sensitivity of the results to the storage pressure and discharge temperature of the high-pressure compressor are discussed as well. We also discuss the thermodynamics of conventional CAES and CAES-LTE to benchmark performance of CAES-HTE and A-CAES. The Appendix A section also includes details on the temperature range of each system component over the storage cycle.

3.1. Thermodynamic Comparison of A-CAES and CAES-HTE

Table 1 lists the parameters used to compare the thermodynamics of A-CAES and CAES-HTE in the base case scenario. We consulted the design parameters of the two existing commercial CAES plants (Huntorf and McIntosh [10,15,33–36]), as well as literature on design of A-CAES systems [15,16,20,31,32,36] to choose these values. In the sensitivity analysis section, we discuss the impact of two key design parameters, cavern storage pressure and discharge temperature of the HP compressor. The simulation results are tabulated in Table 2. Refer to the nomenclature for the list of symbols.

Table 1. Inputs for analysis of the A-CAES and CAES-HTE systems in the base case. The conventional CAES and CAES-LTE systems use the same values with the main exception that the maximum storage pressure is 7 MPa instead of 10 MPa.

Parameter	Value	Parameter	Value	Parameter	Value
γ	1.4	V	0.56 Mm ³	LHV _{H2}	120 MJ/kg
C_p	1.006 $\frac{\text{kJ}}{\text{kg}\cdot\text{K}}$	R	0.287 $\frac{\text{kJ}}{\text{kg}\cdot\text{K}}$	x_{H2}	114 MJ/kg
$P_{CN,fl}$	10 MPa	T_{ac}	30 °C	$T_{in}^{TB,LP}$	850 °C
$P_{CN,em}$	5 MPa	η_{TB}	85%	T_{et}	130 °C
η_{CM}	85%	$T_{in,coolant}^{CL}$	25 °C	$T_{in}^{TB,HP}$	530 °C
$T_{out}^{CM,HP,Max}$	600 °C	$T_{out}^{TS2,ch}$	100 °C		

Table 2. Simulation results for the A-CAES and CAES-HTE systems simulated in the base case scenario.

Variable	A-CAES	CAES-HTE (100% Efficient Electrolyzer)	CAES-HTE (50% Efficient Electrolyzer)
W_{CM} (TJ)	15.22	15.22	15.22
$Q_{electrolysis}$ (TJ)	-	7.96	7.96
$W_{electrolysis}$ (TJ)	-	14.82	29.65
Q_{TS} (TJ)	13.62	-	-
W_{TB} (TJ)	10.58	15.99	15.99
Q_{CC} (TJ)	-	17.59	17.59
$\eta_{storage}$ (%)	69.5	53.2	35.6
WR	1.44	1.88	2.81
ρ (kWh/m ³)	5.2	7.9	7.9

The compression work to fully charge the cavern for both A-CAES and CAES-HTE is the same (15.22 TJ). This is because the compressors in both systems are identical (equal pressure, temperature, and mass of working air). The high temperature electrolyzer of the CAES-HTE system uses 14.83 TJ to produce enough hydrogen for combustion during the discharge phase. The electrolyzer has a heating load of 7.96 TJ to generate steam and electrolyze it. This heat is supplied by the thermal energy dissipated from the compressors. Therefore, about 52% of the compression work is recovered and used in the HTE to produce hydrogen. In the adiabatic system, about 89% of the compression work is physically stored (13.62 GJ). The remainder of heat is released to the ambient environment. Therefore, the A-CAES system recovers and utilizes a higher portion of the energy supplied to the compressor (compression work).

Because the temperature of the expanding air is higher in the CAES-HTE configuration (due to the combustion of hydrogen), the generated work (15.99 TJ) is larger than that of the A-CAES system

(10.58 TJ). The heat load of CAES-HTE combustors is 17.59 TJ. This is while the heat transferred to the expanding air in the A-CAES system is 13.62 TJ (equal to the stored heat).

The A-CAES system is thermodynamically more efficient than the CAES-HTE system based on our analysis. Physical storage of the compression heat leads to an overall storage efficiency of 69.5% (A-CAES) compared to 35.6% for its chemical storage in the form of hydrogen (CAES-HTE, assuming a 50% efficient electrolyzer). The simulated CAES-HTE system uses 29.65 TJ more electricity (to produce hydrogen in the electrolyzer) compared to A-CAES (both systems have the same compression work of 15.22 TJ). The CAES-HTE system however, produces 5.41 TJ of additional work because it combusts hydrogen and the expanding air has a higher temperature. Therefore, for each unit of excess electrical energy used by the CAES-HTE system, roughly 0.18 unit of excess electrical energy is generated. This relatively large gap lowers the overall efficiency of CAES-HTE.

The performance of CAES-HTE would be less attractive in the real world due to the inefficiencies of the electrolyzer itself. The energy efficiency of the electrolysis process can be defined as the ratio of the theoretical electricity demand (ΔG) to the actual use. No commercial large-scale HTE facility currently exists to our knowledge. The efficiency of the laboratory-scale systems are reported as about 50% (at operating temperatures of about 850 °C [37]). To estimate the upper bound of the CAES-HTE performance, we also run the simulation with an ideal electrolyzer (100% efficient). This would halve the work load of the electrolyzer to 14.82 TJ. This decrease in energy consumption improves the roundtrip efficiency of the CAES-HTE system to 53.2% from 35.6%.

The storage requirements of hydrogen are likely to degrade the performance of CAES-HTE too. One would need to compress the hydrogen for storage and use later during the discharge phase in CAES-HTE. We have ignored this additional work load in our analysis.

The hydrogen-based system benefits, however, from a higher exergy density (7.9 kWh/m³) compared to A-CAES (5.2 kWh/m³). This is because the CAES-HTE system stores energy both as mechanical energy (compressed air) and as chemical energy (hydrogen). Thus A-CAES would require 52% more cavern volume to generate the same amount of work in our analysis.

3.2. Sensitivity of A-CAES and CAES-HTE to Exit Temperature of the HP Compressor

We treat the maximum exit temperature of the HP compressor ($T_{out}^{CM,HP,Max}$) as a key design parameter for A-CAES and CAES-HTE. Tables 3 and 4 present the sensitivity of the results to this parameter (all other parameters are similar to the base case scenario, Table 1).

Table 3. Sensitivity of the CAES-HTE results to the maximum exit temperature of the HP compressor ($T_{out}^{CM,HP,Max}$). Results are based on an ideal electrolyzer.

Variable	$T_{out}^{CM,HP,Max}$ (°C)			
	500	600	700	800
W_{CM} (TJ)	14.20	15.22	16.24	17.25
$Q_{electrolysis}$ (TJ)	7.24	7.96	8.70	9.45
$W_{electrolysis}$ (TJ)	15.19	14.83	14.45	14.07
T_{HTE} (°C)	460	555	650	745
$\eta_{storage}$ (%)	54.4	53.2	52.1	51.1

For CAES-HTE, setting a higher exit temperature for the HP compressor translates to a higher inlet temperature for this compressor and a lower cooling load for the LP cooler (because the compression ratio is constant). This provides more thermal energy for the electrolysis process, which reduces its electricity demand to produce the same amount of hydrogen. Nevertheless, as the maximum discharge temperature of the high pressure compressor ($T_{out}^{CM,HP,Max}$) increases from 500 °C to 800 °C, less cooling by the LP cooler increases the work load of the HP compressor (because of the higher inlet temperature of the HP compressor). As shown in Table 3, the net effect of a higher compression work and a lower electrolysis work is an increase in the exergy demand of CAES-HTE to charge the cavern. The total

input exergy (summation of work of compressor and electrolyzer) increases from 29.39 TJ to 31.32 TJ. The discharge phase is insensitive to these changes in our model. Storage efficiency of the CAES-HTE system drops from 54.4% to 51.1% across this range. Results are presented for a CAES-HTE system with an ideal (100% efficient) electrolyzer.

Table 4. Sensitivity of the A-CAES performance to the maximum discharge temperature of the high-pressure compressor ($T_{out}^{CM,HP,Max}$).

Variable	$T_{out}^{CM,HP,Max}$ (°C)			
	500	600	700	800
W_{CM} (TJ)	14.20	15.22	16.24	17.25
Q_{TS} (TJ)	12.60	13.62	14.63	15.65
W_{TB} (TJ)	10.43	10.58	10.61	10.88
$\eta_{storage}$ (%)	73.4	69.5	65.4	63.1
$T_{out}^{TB,HP,Min}$ (°C)	54	26	−8	−31
$T_{out}^{TB,LP,Min}$ (°C)	142	181	217	259

In the A-CAES system, raising $T_{out}^{CM,HP,Max}$ increases the compression work too. This is because less cooling is done in the low pressure cooler and consequently, the inlet temperature to the HP compressor is elevated. At the same time, more heat is stored in TS2 from the air leaving the HP compressor. The turbine's total work increases by about 4% (from 10.43 to 10.88 TJ) as $T_{out}^{CM,HP,Max}$ is raised from 500 to 800 °C. This small increase in the expansion work despite a much higher (24%, from 12.60 to 15.65 TJ) increase in the total thermal energy stored (Q_{TS}) occurs because the thermal energy stored in TS1 (Q_{TS1}) and, consequently, the heat given to the air entering the HP turbine and the work generated by the HP turbine, ought to decrease to allow higher temperatures for the intake and thus discharge of the high pressure compressor. Note that TS1 precedes the HP compressor and HP expander (see Figure 4).

The net effect of increasing $T_{out}^{CM,HP,Max}$ is lowering the storage efficiency of A-CAES. Its efficiency decreases from 73.4% to 63.1% when $T_{out}^{CM,HP,Max}$ increases from 500 to 800 °C. Comparing Table 3 with Table 4 shows that storage efficiency of A-CAES is more sensitive to the temperature of air stream leaving the compressor, compared with that of CAES-HTE.

An important design consideration in our model is the discharge temperature of the expander. This variable needs to remain above the freezing point of water to avoid mechanical damage to the expanders. Referring to Table 4, the exit temperature of the HP turbine drops as $T_{out}^{CM,HP,Max}$ increases. Because less heat can be stored in TS1 and then released to the compressed air entering the high pressure expander. This temperature drops below the freezing point when $T_{out}^{CM,HP,Max}$ reaches 700 °C in our analysis. Designing A-CAES in the real world would need to include a detailed analysis to optimize the performance of the plant and avoid freezing concerns. For instance, although they are constrained to be equal in our model, the HP expander can be designed to have a lower expansion ratio than the LP expander. This will raise and lower the discharge temperatures of the HP and LP expanders, respectively.

3.3. Sensitivity of A-CAES and CAES-HTE to Storage Pressure

The storage pressure of air is our second key design parameter. The sensitivity of the CAES-HTE and A-CAES results to the maximum storage pressure are shown in Tables 5 and 6. All parameters are from Table 1. The maximum cavern pressure is varied in the range of 7–12 MPa, compared to 10 MPa in the base case. The minimum storage pressure is kept at 5 MPa in all cases.

For the CAES-HTE system, the compression work and hydrogen demand increase at higher storage pressures. This is because more air needs to be stored and heated. The operating temperature of the electrolyzer slightly decreases at higher pressures since we keep the maximum discharge

temperature of the high-pressure compressor fixed. Higher cavern pressures translate to higher compression ratios. Keeping the $T_{out}^{CM,HP,Max}$ constant requires a lower inlet temperature for the HP compressor at higher cavern pressures. Therefore, TS1 (preceding the HP compressor) needs to absorb more heat from the compressed air leaving the LP compressor and entering the HP compressor. A lower discharge temperature for the HP compressor decreases the temperature of the air entering the electrolyzer, and thus the electrolysis reaction temperature. This temperature drops from 578 to 544 °C as the maximum storage pressure of air ($P_{CN,fl}$) is raised from 7 to 12 MPa for a CAES-HTE system with an ideal electrolyzer.

Table 5. Sensitivity of the CAES-HTE model to maximum storage pressure. Results are based on an ideal electrolyzer.

Variable	P_{fl} (MPa)			
	7	8	10	12
W_{CM} (TJ)	5.88	8.93	15.22	21.73
$Q_{electrolysis}$ (TJ)	3.15	4.75	7.96	21.15
$W_{electrolysis}$ (TJ)	5.72	8.69	14.82	22.79
T_{HTE} (°C)	578	569	555	544
W_{TB} (TJ)	6.18	9.39	15.99	22.79
Q_{CC} (TJ)	6.82	10.35	17.60	25.03
$\eta_{storage}$ (%)	53.3	53.3	53.2	53.1
ρ (kWh/m ³)	3.1	4.7	7.9	11.3

Table 6. Sensitivity of the A-CAES model to the maximum storage pressure.

Variable	P_{fl} (MPa)			
	7	8	10	12
W_{CM} (TJ)	5.88	8.93	15.22	21.73
Q_{TS} (TJ)	5.24	7.97	13.62	19.48
W_{TB} (TJ)	3.90	6.00	10.58	15.36
$\eta_{storage}$ (%)	66.3	67.2	69.5	70.7
$\rho_{STORAGE}$ (kWh/m ³)	1.9	3.0	5.2	7.6
$T_{out}^{TB,HP,Min}$ (°C)	5	11	26	33

The expansion work increases at higher cavern pressures because more compressed air is handled, and at higher pressures. The net impact of higher cavern pressures on the storage efficiency is negligible (slightly negative). Increased work loads for the compressor and the HTE cancel out the higher expansion work. The exergy density of the cavern increases ~2.7 times as the maximum storage pressure increases from 7 to 12 MPa. Therefore, increasing the cavern pressure substantially improves the exergy density of the plant while it marginally degrades the storage efficiency. In the real world, however, the storage efficiency is likely to degrade more compared to the scenario pictured here. For example, we have assumed a fixed isentropic efficiency for the compressors whereas their efficiency is likely to degrade at higher compression ratios [38].

For the A-CAES system, higher cavern pressures translate to higher compression work as well. At the same time, more waste heat recovery opportunities are available. The expansion work also increases as a larger mass of air and at a higher pressure is expanded. The net effect of higher compression work, recovered heat, and expansion work is positive on the storage efficiency of A-CAES. It rises from 66.3% to 70.7% as the cavern pressure is lifted from 7 to 12 MPa. The exergy density of the cavern at 12 MPa is almost 4 times that of 7 MPa, as more air is stored in the same cavern, and at higher pressures. Finally, the exit temperature of the HP expander is also raised, due to more stored heat despite the higher expansion ratios. This is beneficial in addressing the concerns with freezing of vapor in the expanding air and damaging the turbine blades.

3.4. Thermodynamics of Conventional CAES and CAES-LTE

In Table 7, we present the results for thermodynamics of conventional CAES and CAES-LTE systems. For the most part, we use the same input parameters as for A-CAES and CAES-HTE (Table 1), such as air storage temperature, minimum cavern pressure, and discharge temperature of the final heat exchanger. This is to benchmark the performance of A-CAES and CAES-HTE. The primary difference is that the compression train of CAES and CAES-LTE is made up of three stages. This is because there is no need to generate high temperature heat in these designs. Therefore, more intercooling can be performed to lower the compression work, similar to the McIntosh and Huntorf CAES plants. Moreover, the maximum storage pressure of the cavern is set at 7 MPa instead of 10 MPa, again as high temperature heat is not needed. As the number of compression stages increases and their compression ratio drops, energy losses during the compression (charging) phase decrease. This is because the compression process gets closer to an isothermal instead of an adiabatic process.

Table 7. Simulation results for the conventional CAES and CAES-LTE systems.

Variable	CAES-LTE (100% Efficient Electrolyzer)	CAES-LTE (50% Efficient Electrolyzer)	CAES
W_{CM} (TJ)	4.56	4.56	4.56
$Q_{\text{electrolysis}}$ (TJ)	1.38	1.38	-
$W_{\text{electrolysis}}$ (TJ)	6.47	13.48	-
W_{TB} (TJ)	6.18	6.18	6.18
Q_{CC} (TJ)	6.82	6.82	6.82
η_{storage} (%)	54.7	34.2	54.3
WR	1.83	2.92	0.74
ρ (kWh/m ³)	3.1	3.1	3.1

The storage efficiency of the CAES-LTE system with a 50% efficient electrolyzer is 34.2%, which is comparable to that of the CAES-HTE system. This indicates that the lower electricity demand of the electrolyzer in CAES-HTE system is offset by its higher compression work. Using an ideal (100% efficient) electrolyzer instead of a 50% efficient electrolyzer leads to an overall storage efficiency of 54.7% for CAES-LTE.

The efficiency of the conventional CAES system is 54.3%, which is lower than that of A-CAES (69.5%) and similar to the hydrogen-fueled CAES systems with ideal electrolyzers (53.2% for HTE and 54.7% for LTE). The conventional CAES system has the lowest work ratio (0.74) because it burns natural gas with a heat rate of 3.97 GJ per MWh of gross electricity generated, or 15.27 GJ per MWh of net electricity.

4. Discussion

Our analysis shows that the A-CAES system has the highest exergy storage efficiency, followed by conventional CAES, and then the hydrogen based CAES systems. High exergy losses in electrolyzers constitute a key contributor to the overall low storage efficiency of CAES-HTE and CAES-LTE.

Current literature has identified A-CAES as a potentially important component of low carbon grids with large penetration of renewable energies from an economic point of view. This paper builds on the same premise and provides further insight into thermodynamic performance and competitiveness of A-CAES.

The economics of conventional CAES are likely to be more attractive compared to the other systems studied here unless significant GHG emissions restrictions are in place. The emissions intensity of the conventional CAES system modeled is 262 kgCO₂e/MWh of gross electricity generated whereas the other three systems emit no greenhouse gases. The emissions of the electricity consumed to charge these plants are not included for this calculation. However, if emissions per unit of net rather than gross electricity generated by the CAES plant (generation minus consumption, equal to 1 – WR) is considered, the corresponding emissions intensity is 1008 kgCO₂e/MWh. In other words, the conventional CAES plant would emit 1 metric ton of CO₂e per incremental MWh of electricity

it adds to the grid supply. This is almost 50% higher than that of a simple gas combustion turbine (679 kgCO_{2e}/MWh, using an efficiency of 35% and heat rate of 10.26 GJ/MWh), which competes with storage for filling in the gaps in the supply of intermittent renewables. This high emissions level highlights the shortcoming of the conventional CAES systems in carbon-constrained grids.

Assessing the competitiveness of these storage technologies to support integration of renewable energies into low-carbon grids requires a comprehensive analysis, including both thermodynamics and the economics of practical implementation. Precise thermodynamic assessment of these systems in the real world calls for complex numerical analyses due to their complexities, which is beyond the scope of this paper. Here we offer a few insights into the thermodynamic and economic trade-offs of these systems in the real-world.

Our thermodynamic analysis indicates that prospects for hydrogen-based CAES systems are likely weaker than those of A-CAES due to the lower storage efficiency. Even assuming an ideal electrolyzer leads to storage efficiencies in the lower 50% range as the high end for the CAES-HTE and CAES-LTE configurations studied here, compared to around 70% for A-CAES. Using a currently more realistic electrolyzer efficiency of 50% lowers the overall efficiency of the hydrogen-fueled systems to the mid 30% range. Although thermal losses would decrease the efficiency of A-CAES, they would not be as significant as the electrolyzer losses.

Capital and operating costs of these CAES systems are different, with conventional CAES currently being the most mature and inexpensive for large scale adoption, in the absence of tight emissions restrictions. The design and operation of A-CAES plants are complicated by the need for high-pressure and high-temperature compressors, thermal stores, and high-pressure turbines [31]. In contrast, the engineering and economic complications of high-temperature electrolyzers and hydrogen storage and combustion complicate the CAES-HTE systems. The design and operations of a CAES-LTE system would be simpler because can operate at pressures and temperatures of conventional CAES systems.

Acknowledgments: Hossein Safaei thanks Professor David Keith at Harvard University for the invaluable discussions on CAES systems. Research at Harvard University was partly supported by the Ziff Fund for Energy and Environment.

Author Contributions: H.S. developed the thermodynamic model in collaboration with M.J.A. H.S. and M.J.A. wrote the paper together.

Conflicts of Interest: The authors declare no conflict of interest. The founding sponsors had no role in the design of the study; in the collection, analyses, or interpretation of data; in the writing of the manuscript, and in the decision to publish the results.

Nomenclature

A-CAES	Adiabatic compressed air energy storage
CAES	Compressed air energy storage
CAES-HTE	Compressed air energy storage paired with a high-temperature electrolyzer
CAES-LTE	Compressed air energy storage paired with a low-temperature electrolyzer
CC	Combustor
<i>Ch</i>	Charge process
CL	Cooler (heat exchanger) following compressor stages
C_{Lnt}	Latent heat of evaporation (kJ/kg)
CM	Compressor
CN	Cavern for air storage
coolant	Cold stream of compressor cooler
C_p, C_v	Specific heat at constant pressure and volume ($\frac{\text{kJ}}{\text{kg}\cdot\text{K}}$)
CR	Compression ratio
<i>dch</i>	Discharge process
<i>E</i>	Voltage applied to electrolyzer (volts)
<i>em</i>	State of depleted cavern
<i>et</i>	Exhaust stream of the storage plant

FHX	Heat exchanger located at exhaust of the plant
<i>fl</i>	State of fully charged cavern
<i>G</i>	Gibbs free energy (kJ)
GI	GHG emissions intensity of plant or fuel (kgCO ₂ e/MWh or kgCO ₂ e/GJ, respectively)
<i>h</i>	Specific enthalpy (kJ/kg)
Δh_f^0	Standard enthalpy of formation (kJ/kg)
HP	High-pressure equipment
HR	Heat rate (GJ/MWh)
HTE	High temperature electrolysis/ electrolyzer
<i>in</i>	Inlet conditions
IP	Intermediate-pressure equipment
<i>ist</i>	Isentropic process
IX	Exergy loss (kJ)
LHV	Lower heating value (kJ/kg)
LP	Low-pressure equipment
LTE	Low-temperature electrolysis/ electrolyzer
<i>m</i>	Mass of air or fuel (kg)
<i>M</i>	Molar mass (kg/kMole)
<i>n</i>	Molar coefficient
NG	Natural gas
<i>out</i>	Outlet conditions
<i>P</i>	Pressure (kPa)
<i>Q</i>	Thermal energy (kJ)
<i>R</i>	Ideal gas constant ($\frac{\text{kJ}}{\text{kg}\cdot\text{K}}$)
RP	Recuperator
<i>s</i>	Specific entropy ($\frac{\text{kJ}}{\text{kg}\cdot\text{K}}$)
<i>s</i> ⁰	Standard entropy ($\frac{\text{kJ}}{\text{kg}\cdot\text{K}}$)
<i>S</i>	Entropy (kJ)
<i>sns</i>	Sensible heat (kJ/kg)
<i>T</i>	Temperature
<i>T</i> _{ac}	Approach temperature
TB	Turbine (expander)
TS	Thermal energy storage unit
<i>u</i>	Specific internal energy (kJ/kg)
<i>U</i>	Internal energy (kJ)
<i>V</i>	Volume of air storage (m ³)
<i>W</i>	Work (kJ)
WR	Work ratio
<i>x</i>	Specific exergy (kJ/kg)
<i>X</i>	Exergy (kJ)
XR	Expansion ratio of turbine
ρ	Exergy density of cavern (kWh/m ³)
γ	Specific heat ratio of air
η	Efficiency (%)
ψ	Exergy of air stream (kJ/kg)
0	Standard conditions

Appendix A

We here discuss the details of the analytical models developed to assess the thermodynamics of the compressed air energy storage systems.

We use the following general assumptions and simplifications. One complete charge and discharge cycle is analyzed (without part-load operation). Air is modeled as an ideal gas with temperature-independent specific heat. Mass of the fuel is assumed negligible compared to

the compressed air and the mixture of air and fuel is treated as pure air. Equations (A1)–(A5) list the general ideal gas formulae used. The ambient environment (subscript 0) is at standard conditions ($P_0 = 101$ kPa and $T_0 = 25$ °C). This condition is also the reference state for calculating the internal energy, enthalpy, entropy, and exergy in our analysis.

$$m = \frac{P V}{R T} \quad (\text{A1})$$

$$h = (T - T_0)C_p \quad (\text{A2})$$

$$u = (C_v T) - (C_p T_0) \quad (\text{A3})$$

$$s = C_p \ln\left(\frac{T}{T_0}\right) - R \ln\left(\frac{P}{P_0}\right) \quad (\text{A4})$$

$$\psi = (h - h_0) - (s - s_0)T_0 \quad (\text{A5})$$

In our model, similar to Huntorf and McIntosh CAES plants, the cavern has a fixed volume. Cavern's pressure varies between a minimum pressure (P_{em}) and a maximum (P_{fi}). In order to maintain its mechanical integrity and to ensure high-enough flow rates of the withdrawn air, the cavern is not fully depleted. The air mass remaining in the cavern at the end of the discharge phase (when all the "working air" has been withdrawn to generate electricity) is called the "cushion air".

The cavern and thermal storage units are modeled as adiabatic. The coolers (heat exchangers) following each compressor stage are constrained to have a fixed approach temperature (T_{ac}), defined as the difference between temperature of the cooled compressed air leaving the heat exchanger ($T_{out,air}^{CL}$) and temperature of the coolant ($T_{in,coolant}^{CL}$). This implies the inlet temperature of the cavern and the discharge of all the compressor coolers is constant through the charging process (Equation (A6)).

$$T_{in}^{CN} = T_{out,air}^{CL} = T_{ac} + T_{in,coolant}^{CL} = T_{ac} + T_0 \quad (\text{A6})$$

During the discharge phase, we constrain the exit temperature of the combustors at a fixed value (e.g., through controlling fuel combustion). The expander (turbine) has two stages; high-pressure (HP) and low-pressure (LP). These stages are constrained to have equal but variable expansion ratios (Equation (A7)), according to the instantaneous pressure of the cavern.

$$XR_{HP} = XR_{LP} = \sqrt{\frac{P_0}{P_{CN}}} = \sqrt{XR} \quad (\text{A7})$$

Temperature of the air stream leaving the storage plant (T_{et}) is set to be fixed. An imaginary heat exchanger (FHX) is placed at the exhaust of the storage plant to account for the exergy loss of the exhaust stream to the ambient environment. This heat exchanger cools the air leaving the LP turbine or recuperator, from T_{et} down to the ambient temperature (see Figure 3).

The heat flows (Q) are reckoned to be positive if they enter the system (e.g., heat added in the combustor, Q_{CC}) and negative if they leave the system (e.g., heat dissipated in the compressor coolers, Q_{HC}). The work (W) done by the system on the surroundings has a positive sign (e.g., expansion work, W_{TB}) whereas the work done on the system has a negative sign (e.g., compression work, W_{CM}).

A.1. Thermodynamic Modeling of Conventional CAES

In the conventional CAES system (Figure 3), air is compressed in a multi-stage compressor (CM) and then stored in the cavern (CN). Each compression stage is followed by a heat exchanger (cooler, CL) to reduce compression work of the succeeding stage and to reduce the volumetric requirements for air storage. The compression heat (heat absorbed by the coolers) is rejected to the ambient environment.

We model the compressor of conventional CAES system to have three stages: low-pressure (LP), intermediate-pressure (IP), and high-pressure (HP). All the stages have variable but equal compression ratios and a fixed isentropic efficiency throughout the entire charging process. The compression ratio (CR) varies to match the instantaneous pressure of the cavern (P_{CN}) (see Equation (A8)).

$$CR_{HP} = CR_{IP} = CR_{LP} = \sqrt[3]{\frac{P_{CN}}{P_0}} = \sqrt[3]{CR} \quad (A8)$$

During the discharge phase, air is preheated in a recuperator. It is then combusted with natural gas (NG) and generates work in the expanders (TB). We model a two-stage expander. In the recuperator, the exhaust of the low-pressure (LP) turbine preheats the air entering the high-pressure (HP) combustor.

The two existing commercial CAES plants (Huntorf and McIntosh) have a similar configuration as the one modeled here, except that the Huntorf facility does not utilize a recuperator.

A.1.1. Charge Phase of Conventional CAES

At the beginning of each charging phase, the initial temperature (T_{em}) and pressure (P_{em}) of the cavern are known from the previous storage cycle. Therefore, the mass of the cushion air is calculated by applying the ideal gas equation of state. The relationship between changes in the mass of air present in the cavern ($dm_{air, ch}$) and its instantaneous pressure (P_{ch}) is found by applying the First Law of thermodynamics to the control volume of the cavern (Equation (A9)).

$$dQ - dW = dU_{CV} - h_{air, in} dm_{air, ch} \quad (A9)$$

Since the cavern is adiabatic and has a fixed volume, $dQ = dW = 0$. Using Equations (A1)–(A3), the above equation is transformed into Equation (A10).

$$dm_{air, ch} = \frac{dP_{ch} V}{R \gamma T_{in}^{CN}} \quad (A10)$$

Because the inlet temperature of the cavern (T_{in}^{CN}) is fixed and known, Equation (A10) is integrated to find the total mass of working air ($m_{air, ch}$) as the cavern is charged and its pressure raises from P_{em} to P_{fl} (Equation (A11)). Once the mass of air in the fully charged cavern ($m_{air, fl}$) is determined (Equation (A12)), its temperature ($T_{CN, fl}$) is calculated by applying the ideal gas equation of state (Equation (A13)).

$$m_{air, ch} = \frac{(P_{fl} - P_{em}) V}{R \gamma T_{in}^{CN}} \quad (A11)$$

$$m_{air, fl} = m_{air, em} + m_{air, ch} \quad (A12)$$

$$T_{CN, fl} = \frac{T_{em} P_{fl}}{P_{em} + (P_{fl} - P_{em}) \frac{T_{em}}{\gamma T_{in}^{CN}}} \quad (A13)$$

The compression work for charging the cavern is quantified by applying the First Law of thermodynamics to each compression stage and summing them up (Equation (A14)). Work of the low-pressure compressor is formulated in Equation (A15). A similar equation is applicable to the intermediate-pressure and high-pressure compressors. The inlet temperature of each stage is fixed and known. The instantaneous discharge temperature of each compressor stage is determined by applying the isentropic compression formulae (see Equation (A16) for the LP compressor).

$$W_{CM} = \int_{P_{em}}^{P_{fl}} (dW_{CM, LP} + dW_{CM, IP} + dW_{CM, HP}) \quad (A14)$$

$$dW_{CM,LP} = C_p \left(T_{in}^{CM,LP} - T_{out}^{CM,LP} \right) dm_{air,ch} \quad (A15)$$

$$T_{out}^{CM,LP} = T_{in}^{CM,LP} - \frac{T_{in}^{CM,LP} - T_{out,ist}^{CM,LP}}{\eta_{CM}} \quad (A16)$$

$$T_{out,ist}^{CM,LP} = T_{in}^{CM,LP} CR_{LP}^{(\gamma-1)/\gamma}$$

The total compression heat is determined by applying the First Law of thermodynamics to each compressor cooler and integration (Equation (A17)). As a case in point, Equation (A18) quantifies an increment of heat dissipated by the cooler of the HP compressor. Note the inlet temperature of each cooler equals the discharge temperature of the preceding compression stage. The discharge temperature of the coolers is set to be fixed (Equation (A6)).

$$Q_{CL} = \int_{P_{em}}^{P_{fl}} (dQ_{CL,LP} + dQ_{CL,IP} + dQ_{CL,HP}) \quad (A17)$$

$$dQ_{CL,LP} = C_p \left(T_{out}^{CL,LP} - T_{in}^{CL,LP} \right) dm_{air,ch} \quad (A18)$$

Once the initial (*em*) and final (*fl*) states of the cavern over the charging phase in addition to the compression work are determined, the change in internal energy (ΔU_{ch}), entropy (ΔS_{ch}), and exergy (ΔX_{ch}) of the cavern as well as the exergy loss (IX_{ch}) are calculated with Equations (A19)–(A22).

$$\Delta U_{ch} = m_{air,fl} u_{fl} - m_{air,em} u_{em} \quad (A19)$$

$$\Delta S_{ch} = m_{air,fl} s_{fl} - m_{air,em} s_{em} \quad (A20)$$

$$\Delta X_{ch} = \Delta U_{ch} - T_0 \Delta S_{ch} \quad (A21)$$

$$IX_{ch} = -\Delta X_{ch} - W_{CM} + m_{air,ch} \psi_{air,ch} \quad (A22)$$

since air entering the system is at ambient conditions, $\psi_{air,ch} = 0$.

A.1.2. Discharge Phase of Conventional CAES

Similar to the charging process, we use the First Law of thermodynamics to find the relationship between the instantaneous temperature and changes in the mass and pressure of the air present in the cavern during the discharge phase (Equation (A23)).

$$dm_{air,dch} = \frac{dP_{CN} V}{R \gamma T_{CN}} \quad (A23)$$

Using Equation (A23) and the state equation for ideal gas, mass of air left in the cavern at the end of the discharge process (cushion air, $m_{air,em}$) and total mass of air withdrawn (working air, $m_{air,dch}$) are calculated via Equations (A24) and (A25).

$$\frac{dm_{air,dch}}{m_{air,dch}} = \frac{dP_{CN}}{\gamma P_{CN}}$$

$$m_{air,em} = m_{air,fl} \left(\frac{P_{em}}{P_{fl}} \right)^{\frac{1}{\gamma}} \quad (A24)$$

$$m_{air,dch} = m_{air,fl} - m_{air,em} = \frac{V}{R} \left(\frac{P_{em}}{T_{em}} + \frac{P_{fl} - P_{em}}{\gamma T_{in}^{CN}} \right) \left(1 - \left(\frac{P_{em}}{P_{fl}} \right)^{\frac{1}{\gamma}} \right) \quad (A25)$$

Now that mass of the cushion air is known (Equation (A24)), the state equation is applied to determine the instantaneous and final temperature of the compressed air in the cavern (Equations (A26) and (A27)).

$$T_{CN, dch} = T_{fl} \left(\frac{P_{CV}}{P_{fl}} \right)^{(\gamma-1)/\gamma} \quad (\text{A26})$$

$$T_{em} = T_{fl} \left(\frac{P_{em}}{P_{fl}} \right)^{(\gamma-1)/\gamma} \quad (\text{A27})$$

The initial temperature of air in the fully discharged cavern is set to T_0 (i.e., temperature of the air in cavern at the beginning of the very first cycle). This temperature eventually reaches asymptotic limits after many cycles, regardless of the initial temperature we choose. Simulation is run until this asymptotic limit is reached and all the results are reported then.

Temperature of the air entering the low- and high-pressure turbines ($T_{in}^{TB,LP}$ and $T_{in}^{TB,HP}$) is set fixed and constant in the analysis. However, the discharge temperature varies according to the instantaneous expansion ratio, which is itself a function of the instantaneous cavern pressure. The First Law of thermodynamics is applied to each expander stage to find the work generated (Equations (A28) and (A29)). The instantaneous discharge temperature of the high-pressure expander is quantified by Equation (A30), based on the isentropic expansion formulae. A similar set of equations can be written for the low-pressure turbine. We use a fixed isentropic efficiency for all stages.

$$W_{TB} = \int_{P_{fl}}^{P_{em}} (dW_{TB,HP} + dW_{TB,LP}) \quad (\text{A28})$$

$$dW_{TB,HP} = C_p \left(T_{in}^{TB,HP} - T_{out}^{TB,HP} \right) dm_{air,dch} \quad (\text{A29})$$

$$T_{out}^{TB,HP} = T_{in}^{TB,HP} + \eta_{TB} \left(T_{out,ist}^{TB,HP} - T_{in}^{TB,HP} \right) \quad (\text{A30})$$

$$T_{out,ist}^{TB,HP} = T_{in}^{TB,HP} X_{R_{HP}}^{(\gamma-1)/\gamma}$$

Once the instantaneous exit temperature of the high-pressure expander ($T_{out}^{TB,HP}$) is quantified, total heat added in the low-pressure combustor is determined by applying the First Law of thermodynamics (Equation (A31)). Note that $T_{in}^{CC,LP} = T_{out}^{TB,HP}$ and $T_{out}^{CC,LP} = T_{in}^{TB,LP}$.

$$Q_{CC,LP} = \int_{P_{fl}}^{P_{em}} C_p \left(T_{out}^{CC,LP} - T_{in}^{CC,LP} \right) dm_{air,dch} \quad (\text{A31})$$

The instantaneous temperature of air entering the high-pressure combustor is expressed as a function of the cavern's pressure by applying the First Law of thermodynamics to the recuperator (Equation (A32)). Similar to the low-pressure combustor, the heat added in the high-pressure combustor is quantified by applying the First Law of thermodynamics (see Equation (A33)). Note that $T_{in}^{CC,HP} = T_{out,coolant}^{RP}$ and $T_{out}^{CC,HP} = T_{in}^{TB,HP}$. T_{et} is the fixed temperature of the exhaust stream of the plant, which is leaving the recuperator (RP) and entering the final heat exchanger (FHX).

$$T_{in}^{CC,HP} = T_{CN, dch} + T_{out}^{TB,LP} - T_{et} \quad (\text{A32})$$

$$Q_{CC,HP} = \int_{P_{fl}}^{P_{em}} C_p \left(T_{out}^{CC,HP} - T_{in}^{CC,HP} \right) dm_{air,dch} \quad (\text{A33})$$

Once the heat added in the combustor is known, the total mass and exergy of the fuel (natural gas) are quantified (Equations (A34) and (A35)).

$$m_{NG} = \frac{Q_{LP,CC} + Q_{HP,CC}}{LHV_{NG}} \quad (A34)$$

$$X_{NG} = m_{NG} x_{NG} \quad (A35)$$

The First Law of thermodynamics is applied to quantify the heat recovered in the recuperator and the heat dissipated in the final heat exchanger (Equations (A36) and (A37)).

$$Q_{RP} = \int_{P_{fl}}^{P_{em}} C_p (T_{et} - T_{out}^{TB,LP}) dm_{air,dch} \quad (A36)$$

$$Q_{FHX} = \int_{P_{fl}}^{P_{em}} C_p (T_0 - T_{et}) dm_{air,dch} \quad (A37)$$

Finally, the change in internal energy, entropy, and exergy of the cavern as well as exergy lost over the discharge process are calculated (Equation (A38) to Equation (A41)). The exergy of air stream leaving the storage plant ($\psi_{air,dch}$) is zero, similar to the exergy of air entering the plant ($\psi_{air,ch}$). This is because both air streams are at ambient conditions.

$$\Delta U_{dch} = m_{air,em} u_{em} - m_{air,fl} u_{fl} \quad (A38)$$

$$\Delta S_{dch} = m_{air,em} s_{em} - m_{air,fl} s_{fl} \quad (A39)$$

$$\Delta X_{dch} = \Delta U_{dch} - T_0 \Delta S_{dch} \quad (A40)$$

$$IX_{dch} = -\Delta X_{dch} - W_{TB} + X_{NG} - m_{air,dch} \psi_{air,dch} \quad (A41)$$

A.1.3. Roundtrip Analysis of Conventional CAES

Once the work, heat, and exergy fluxes during the charge and discharge processes are quantified, the storage efficiency, work ratio and heat rate of the storage plant are calculated (Equation (A42) to Equation (A44)). The GHG emissions intensity of the plant and cavern exergy density are determined by using Equations (A45) and (A46).

$$\eta_{storage} = \frac{W_{TB}}{-W_{CM} + X_{NG} - W_{electrolysis}} \quad (A42)$$

$$WR = \frac{-W_{CM} - W_{electrolysis}}{W_{TB}} \quad (A43)$$

$$HR = \left(\frac{m_{NG} LHV_{NG}}{W_{TB}} \right) \left(\frac{3.6 \text{ GJ}}{\text{MWh}} \right) \quad (A44)$$

$$GI_{storage} = (HR) (GI_{NG}) \quad (A45)$$

$$\rho = \frac{W_{TB}}{V} \quad (A46)$$

We use an emissions intensity of 66 kgCO₂e/GJ for natural gas to account for upstream emissions in addition to combustion emissions [2].

Figure A1 illustrates the temperature range for each system component over the full charge and discharge cycle. In parentheses by each component are the minimum and maximum temperatures in °C as the plant goes through a full charging and discharge cycle. For instance (39,70) at the discharge of the cavern indicates the temperature of the fully discharged cavern (39 °C at 5 MPa) and fully

The compression work of A-CAES is calculated by applying the First Law of thermodynamics to the LP and HP compressors and summing them up (Equation (A48)). The work and discharge temperature of the LP compressor are quantified by Equations (A49) and (A50). Similar formulae can be written for the HP compressor.

$$W_{CM} = \int_{P_{em}}^{P_{fl}} (dW_{CM,LP} + dW_{CM,HP}) \quad (A48)$$

$$dW_{CM,LP} = C_p \left(T_{in}^{CM,LP} - T_{out}^{CM,LP} \right) dm_{ch} \quad (A49)$$

$$T_{out}^{CM,LP} = T_{in}^{CM,LP} - \frac{T_{in}^{CM,LP} - T_{out,ist}^{CM,LP}}{\eta_{CM}} \quad (A50)$$

$$T_{out,ist}^{CM,LP} = T_{in}^{CM,LP} CR_{LP}^{(\gamma-1)/\gamma}$$

The maximum exit temperature of the high-pressure compressor is a preset parameter, which will be varied in the sensitivity analysis section. Our rationale for this design constraint is the following. The exit temperature of the compressor is a key parameter for determining the exergy supplied to and stored in thermal storage. This consequently impacts the temperature of the air entering the expanders during the discharge phase. Moreover, there are technical constraints such as the stress on and the fatigue of compressor blades driven by the maximum temperature of the compressor.

Thermal storage units (TS1 and TS2) are constrained to have a constant discharge temperature over the charging period. The constant exit temperature of TS2 (succeeding the HP compressor) is preset ($T_{out}^{TS2,ch}$). The constant exit temperature of TS1 (preceding the HP compressor) is, however, dictated by the value chosen for maximum discharge temperature of the HP compressor ($T_{out}^{CM,HP,Max}$). Solving the system of equations composed of Equations (A51)–(A53) finds the fixed inlet temperature of the high-pressure compressor ($T_{in}^{CM,HP}$) that limits its maximum exit temperature to the preset value of $T_{out}^{CM,HP,Max}$. Note that $T_{in}^{CM,HP}$ is equal to $T_{out}^{TS1,ch}$.

$$CR_{HP,Max} = \sqrt[2]{\frac{P_{fl}}{P_0}} = \sqrt[2]{CR_{Max}} \quad (A51)$$

$$T_{out}^{CM,HP,Max} = T_{in}^{CM,HP} + \frac{T_{out,ist}^{CM,HP,Max} - T_{in}^{CM,HP}}{\eta_{CM}} \quad (A52)$$

$$T_{out,ist}^{CM,HP,Max} = T_{in}^{CM,HP} (CR_{HP,Max})^{\frac{\gamma-1}{\gamma}} \quad (A53)$$

Equation (A54) gives the total heat stored in TS2 during the charging phase. The inlet temperature of TS2 is equal to the exit temperature of the high-pressure compressor and is a function of the instantaneous compression ratio (see Equations (A55) and (A56)). The exit temperature of TS2 ($T_{out}^{TS2,ch}$) is constrained to be constant throughout the charging process. Equations (A57)–(A59) show similar formulae for TS1 absorbing and storing the heat from compressed air leaving the LP compressor.

$$Q_{TS2,ch} = \int_{P_{em}}^{P_{fl}} C_p \left(T_{out}^{TS2,ch} - T_{out}^{CM,HP} \right) dm_{air,ch} \quad (A54)$$

$$T_{out}^{CM,HP} = T_{in}^{CM,HP} - \frac{T_{in}^{CM,HP} - T_{out,ist}^{CM,HP}}{\eta_{CM}} \quad (A55)$$

$$T_{out,ist}^{CM,HP} = T_{in}^{CM,HP} (CR_{HP})^{\frac{\gamma-1}{\gamma}} \quad (A56)$$

$$Q_{TS1,ch} = \int_{P_{em}}^{P_{fl}} C_p \left(T_{out}^{TS1,ch} - T_{out}^{CM,LP} \right) dm_{air,ch} \quad (A57)$$

$$T_{out}^{CM,LP} = T_{in}^{CM,LP} - \frac{T_{in}^{CM,LP} - T_{out,ist}^{CM,LP}}{\eta_{CM}} \quad (A58)$$

$$T_{out,ist}^{CM,LP} = T_{in}^{CM,LP} (CR_{LP})^{\frac{\gamma-1}{\gamma}} \quad (A59)$$

Exergy of the heat stored in TS1 and TS2 is similarly quantified (Equations (A60) and (A61)). The exergy of the air stream is calculated according to Equations (A2), (A4) and (A5) since the inlet and outlet temperature and pressure of TS1 and TS2 are known.

$$\Delta X_{TS1,ch} = \int_{P_{em}}^{P_{fl}} \left(\psi_{out}^{TS1,ch} - \psi_{out}^{CM,LP} \right) dm_{air,ch} \quad (A60)$$

$$\Delta X_{TS2,ch} = \int_{P_{em}}^{P_{fl}} \left(\psi_{out}^{TS2,ch} - \psi_{out}^{CM,HP} \right) dm_{air,ch} \quad (A61)$$

Air stream leaving TS2 is further cooled in the aftercooler prior to entering the cavern. Equation (A62) quantifies the heat rejected to the ambient in the aftercooler. Equation (A63) expresses the total heat that is dissipated by the compressor, equal to the heat stored by TS1 and TS2 plus the heat rejected to the ambient environment by the aftercooler

$$Q_{CL} = \int_{P_{em}}^{P_{fl}} C_p \left(T_{in}^{CN} - T_{out}^{TS2,ch} \right) dm_{air,ch} \quad (A62)$$

$$Q_{CM} = Q_{CL} + Q_{TS1,ch} + Q_{TS2,ch} \quad (A63)$$

Equations (A19)–(A21) remain applicable for quantifying the changes in the internal energy, entropy, and exergy of the air stored in the cavern of A-CAES. Exergy destroyed over the charging period is shown in Equation (A64).

$$IX_{ch} = -\Delta X_{ch} - W_{CM} + m_{ch} \psi_0 - \Delta X_{TS1,ch} - \Delta X_{TS2,ch} \quad (A64)$$

A.2.2. Discharge Phase of A-CAES

Changes in the mass and temperature of compressed air present in the cavern of A-CAES during the discharge period are expressed by Equations (A23)–(A27), similar to the conventional CAES model.

We assume perfect storage of heat, i.e., all the thermal energy stored during the charging phase is released back to the expanding air without any losses. The exit temperature of TS1 and TS2 is assumed to remain constant over the discharge period.

The First Law of thermodynamics is applied to perform a series of trials and errors in order to find the fixed (but unknown) exit temperature of TS1 so that the heat released by TS1 during the discharge period (Equation (A65)) becomes equal to the heat previously stored in it during the charge period (Equation (A57)).

$$Q_{TS1,dch} = \int_{P_{fl}}^{P_{em}} C_p \left(T_{out}^{TS1,dch} - T_{CN,dch} \right) dm_{air,dch} \quad (A65)$$

$T_{CN,dch}$ is the instantaneous temperature of air leaving the cavern (Equation (A26)).

Once the exit temperature of TS1 is calculated, work and discharge temperature of the high-pressure expander are found through applying the First Law of thermodynamics to the high-pressure expander (Equations (A66) and (A67)). The instantaneous expansion ratio is expressed by Equation (A7).

$$W_{TB,HP} = \int_{P_{fl}}^{P_{em}} C_p \left(T_{out}^{TS1,dch} - T_{out}^{TB,HP} \right) dm_{air,dch} \quad (A66)$$

$$T_{out}^{TB,HP} = T_{out}^{TS1,dch} + \eta_{TB} \left(T_{out,ist}^{TB,HP} - T_{out}^{TS1,dch} \right) \quad (A67)$$

$$T_{out, ist}^{TB,HP} = \left(T_{out}^{TS1,dch} \right) XR_{HP}^{(\gamma-1)/\gamma}$$

Upon determining the intake temperature of TS2 during the discharge phase (equal to $T_{out}^{TB,HP}$), we again use the First Law of thermodynamics to express heat of TS2 during the discharge phase (Equation (A68)). The same trial and error procedure explained for TS1 is applied to Equations (A68) and (A54) to find the exit temperature of TS2.

$$Q_{TS2,dch} = \int_{P_{fl}}^{P_{em}} C_p \left(T_{out}^{TS2,dch} - T_{out}^{TB,HP} \right) dm_{air,dch} \quad (A68)$$

The changes in the exergy stock of TS1 and TS2 are quantified by Equations (A69) and (A70). Since we model the thermal storage systems as ideal (no losses), the exergy released by TS1 and TS2 is equal to the exergy stored during the charging phase.

$$\Delta X_{TS1,dch} = \int_{P_{em}}^{P_{fl}} \left(\psi_{out}^{TS1,dch} - \psi_{dch}^{CN} \right) dm_{air,dch} \quad (A69)$$

$$\Delta X_{TS2,dch} = \int_{P_{em}}^{P_{fl}} \left(\psi_{out}^{TS2,dch} - \psi_{out}^{TB,HP} \right) dm_{air,dch} \quad (A70)$$

Now that the inlet temperature of the low-pressure turbine is determined (equal to discharge temperature of TS2), the First Law of thermodynamics is used to determine the work of the low-pressure turbine (Equation (A71)) and its exit temperature (Equation (A72)).

$$W_{TB,LP} = \int_{P_{fl}}^{P_{em}} C_p \left(T_{out}^{TS2,dch} - T_{out}^{TB,LP} \right) dm_{air,dch} \quad (A71)$$

$$T_{out}^{TB,LP} = T_{out}^{TS2,dch} + \eta_{TB} \left(T_{out, ist}^{TB,LP} - T_{out}^{TS2,dch} \right) \quad (A72)$$

$$T_{out, ist}^{TB,LP} = \left(T_{out}^{TS2,dch} \right) \left(XR_{LP}^{(\gamma-1)/\gamma} \right)$$

Finally, we quantify the heat dissipated by the final exhaust heat exchanger via Equation (A73).

$$Q_{FHX} = \int_{P_{fl}}^{P_{em}} C_p \left(T_0 - T_{out}^{TB,LP} \right) dm_{air,dch} \quad (A73)$$

Equations (A38)–(A40) remain applicable to calculate the changes in the internal energy, entropy, and exergy of cavern over the discharge phase. Equation (A74) quantifies the total exergy loss during the discharge phase of A-CAES.

$$IX_{dch} = -\Delta X_{dch} - W_{TB} - m_{air,dch} \psi_{air,dch} - \Delta X_{TS1,dch} - \Delta X_{TS2,dch} \quad (A74)$$

A.2.3. Roundtrip Analysis of A-CAES

Equations (A42)–(A46) are applicable for the performance of the A-CAES system. Since no fuel is consumed, the heat rate and GHG emissions intensity of A-CAES are zero.

Similar to Figure A1, Figure A2 shows the temperature range for each A-CAES system components over the storage cycle.

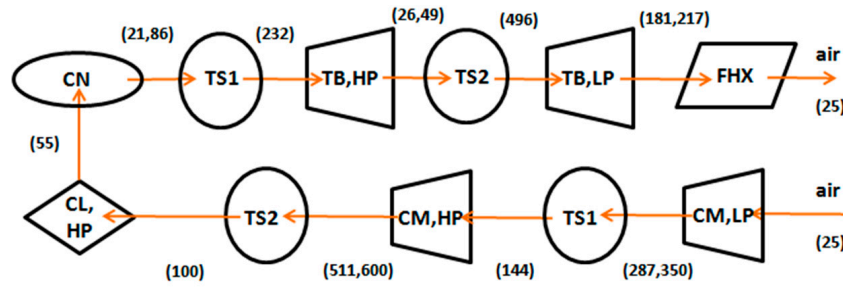


Figure A2. Temperature range of the A-CAES system in the base case scenario. Values in each bracket show minimum and maximum temperature. The cavern operates in 5–10 MPa range. The compressor and expander stages have equal pressure ratios.

A.3. Modeling CAES Paired with a High-Temperature Electrolyzer

The compressor of the CAES-HTE system simulated has two stages (similar to A-CAES). A cooler (heat exchanger) lowers the temperature of the exhaust stream of the LP compressor to a fixed value before entering the high-pressure compressor. The maximum discharge temperature of the high-pressure compressor is a design parameter and is preset, similar to A-CAES. The discharge of the HP compressor is fed into a high-temperature electrolyzer. Its heat is used to boil water, to heat up the generated steam to the constant temperature of the electrolyzer (T_{HTE}), and to provide the heating energy required for the electrolysis process.

A cooler follows the electrolyzer, lowering temperature of the compressed air to a fixed value ($T_{CN, in}$) before storage in the cavern. The generated hydrogen is stored separately to combust and heat the expanding air during the discharge phase. No physical storage of heat is performed, in contrast to the A-CAES configuration.

The discharge phase of CAES-HTE is identical to that of the conventional CAES in our model, with the distinction that hydrogen fuels the combustors instead of natural gas.

The heating loads of the high-pressure and low-pressure combustors during the discharge phase determine the amount of hydrogen fuel needed and consequently the energy demand of the electrolyzer during the charge phase. We therefore, discuss the discharging phase first and then the charging phase.

A.3.1. Discharge Phase of CAES-HTE

Equations (A23)–(A27) remain applicable for quantifying the changes in the mass and temperature of the compressed air remaining in the cavern during discharge. Similar to the conventional CAES system, the inlet temperatures of the low-pressure and high-pressure turbines ($T_{in}^{TB,LP}$ and $T_{in}^{TB,HP}$) are preset. Therefore, Equations (A28)–(A30) quantify the expansion work and the instantaneous exit temperature of the turbines (expanders). The heat load of the low-pressure and high-pressure combustors are determined by applying Equations (A31), (A33) and (A75). Finally, the mass and exergy of the hydrogen fuel needed are calculated via Equations (A76) and (A77).

$$Q_{CC} = Q_{LP,CC} + Q_{HP,CC} \quad (A75)$$

$$m_{H2} = \frac{Q_{CC}}{LHV_{H2}} \quad (A76)$$

$$X_{H2} = m_{H2} x_{H2} \quad (A77)$$

Equations (A38)–(A40) remain applicable for quantifying the changes in internal energy, entropy, and exergy of the compressed air present in the cavern. The exergy lost during the discharge phase is quantified by Equation (A78).

$$I_{dch} = -\Delta X_{dch} - W_{TB} + X_{H2}^{CC} - m_{air,dch} \psi_{air,dch} \quad (A78)$$

A.3.2. Charge Phase of CAES-HTE

Charging phase of CAES-HTE is similar to that of conventional CAES with the key difference that exhaust stream of the HP compressor transfers some of its heat to an electrolyzer to generate hydrogen and the rest to the ambient in an aftercooler. As with the A-CAES simulation, the maximum discharge temperature of the HP compressor is preset. This parameter dictates the exit temperature of the LP cooler (a constant but unknown parameter).

Equation (A9) to Equation (A13) remain valid for quantifying changes in the mass and temperature of compressed air in the cavern during the charge period. Work by the LP compressor and its discharge temperature are calculated by applying the First Law of thermodynamics to the low-pressure compressor (Equations (A79) and (A80)).

$$W_{CM,LP} = \int_{P_{em}}^{P_f} C_p (T_{in}^{CM,LP} - T_{out}^{CM,LP}) dm_{air,ch} \quad (A79)$$

$$T_{out}^{CM,LP} = T_{in}^{CM,LP} - \frac{T_{in}^{CM,LP} - T_{out,ist}^{CM,LP}}{\eta_{CM}} \quad (A80)$$

$$T_{out,ist}^{CM,LP} = T_{in}^{CM,LP} CR_{LP}^{(\gamma-1)/\gamma}$$

The next step after quantifying the inlet temperature of the LP cooler (equal to exit temperature of the LP compressor, Equation (A80)) is finding its discharge temperature, which is same as the inlet temperature of the HP compressor. This temperature is constrained to remain constant during the charging period. Its value, however, is dictated by another design parameter: the maximum exit temperature of the HP compressor. Similar to the A-CAES model, solving the system of equations of Equations (A51)–(A53) finds the inlet temperature of the high-pressure compressor ($T_{in}^{CM,HP}$, which is equal to $T_{out}^{CL,LP}$).

Once the inlet temperature of the HP compressor is known, its work and instantaneous exit temperature are determined by applying Equations (A81) and (A82).

$$W_{CM,HP} = \int_{P_{em}}^{P_{fl}} C_p (T_{in}^{CM,HP} - T_{out}^{CM,HP}) dm_{air,ch} \quad (A81)$$

$$T_{out}^{CM,HP} = T_{in}^{CM,HP} - \frac{T_{in}^{CM,HP} - T_{out,ist}^{CM,HP}}{\eta_{CM}} \quad (A82)$$

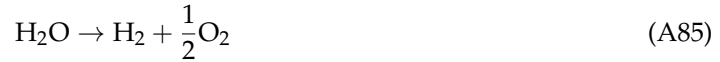
$$T_{out,ist}^{CM,HP} = T_{in}^{CM,HP} CR_{HP}^{(\gamma-1)/\gamma}$$

As illustrated in Figure 2, the energy demand of the electrolyzer depends on the reaction temperature. For the sake of simplicity, we assume a fixed electrolysis temperature, equal to the average exit temperature of the HP compressor over the charge process.

Since the instantaneous inlet temperature of the electrolyzer is known as a function of the compression ratio (equal to $T_{out}^{CM,HP}$, Equation (A82)), one can apply the First Law of thermodynamics to the electrolyzer to find its exit temperature (T_{out}^{HTE}), which results in the desired heat load of the electrolyzer ($Q_{HTE, total}$, quantified in the next paragraphs and expressed by Equation (A97)). A trial and error process is used (similar to the A-CAES system) to find T_{out}^{HTE} .

Total heat demand of the electrolyzer ($Q_{HTE, total}$) is dictated by the mass of hydrogen needed to fuel the combustors during the discharge process. This heating load is made up of four components: sensible heat load to bring water to 100 °C ($Q_{Sns,water}$), latent heat load to boil it ($Q_{Lnt,water}$), sensible heat load to bring the steam from 100 °C to the electrolysis temperature ($Q_{Sns,steam}$), and the heat required for the electrolysis process itself (Q_{HTE}).

In a high-temperature electrolyzer, steam is disassociated in the cathode to produce hydrogen and O^{2-} while O^{2-} gets oxidized in the anode producing oxygen (Equations (A83)–(A85)).



One mole of hydrogen and half a mole of oxygen are generated per mole of water. The relationship between mass of hydrogen and water are shown in Equation (A86).

$$m_{H_2O} = m_{H_2} \left(\frac{M_{H_2O}}{M_{H_2}} \right) \left(\frac{n_{H_2O}}{n_{H_2}} \right) \quad (A86)$$

The sensible heat load of water, sensible heat load of steam, and the latent heat are quantified by Equations (A87)–(A89).

$$Q_{Sns,water} = m_{H_2O} C_p (T_{boil} - T_0) \quad (A87)$$

$$Q_{Sns,steam} = m_{H_2O}^{HTE} C_p (T_{HTE} - T_{boil}) \quad (A88)$$

$$Q_{Ltn,water} = m_{H_2O}^{HTE} C_{Lnt} \quad (A89)$$

For the electrolysis process itself, the total energy requirement (ΔH), the change in entropy (ΔS), and the electricity demand (change in the Gibbs free energy, ΔG) are determined by Equations (A90)–(A92) as a function of the reaction temperature (T).

$$\Delta H_{HTE}(T) = n_{H_2} \Delta h_{H_2}(T) + n_{O_2} \Delta h_{O_2}(T) - n_{H_2O} \Delta h_{H_2O}(T) \quad (A90)$$

$$\Delta S_{HTE}(T) = n_{H_2} \Delta s_{H_2}(T) + n_{O_2} \Delta s_{O_2}(T) - n_{H_2O} \Delta s_{H_2O}(T) \quad (A91)$$

$$\Delta G_{HTE}(T) = \Delta H_{HTE}(T) - T_{HTE} \Delta S_{HTE}(T) \quad (A92)$$

The changes in specific enthalpy (Δh) and entropy (Δs) of the reactant and products are expressed by Equations (A93) and (A94), respectively. Symbols Δh_f^0 and s^0 represent the standard specific enthalpy of formation and the standard specific entropy. Specific heat (c_p) is itself a function of temperature. The values for the standard enthalpy of formation, standard entropy, and specific heat of water and steam are shown in Table A1.

$$\Delta h(T) = \Delta h_f^0 + \int_{T_0}^{T_{HTE}} C_p(T) dT \quad (A93)$$

$$\Delta s(T) = s^0 + \int_{T_0}^{T_{HTE}} \frac{C_p(T)}{T} dT \quad (A94)$$

We therefore, use Table A1 and Equations (A90)–(A94) to quantify the heat and work load of the electrolyzer, as shown in Equations (A95) and (A96).

$$Q_{HTE} = T_{HTE} \Delta S_{HTE}(@T_{HTE}) \quad (A95)$$

$$W_{HTE} = \Delta G_{HTE}(@T_{HTE}) \quad (A96)$$

Finally, the total heat load of the electrolyzer ($Q_{HTE, total}$) is determined by Equation (A97). This variable is used to find the discharge temperature of the electrolyzer (T_{out}^{HTE}) through the trial and error procedure explained earlier.

$$Q_{HTE, total} = Q_{Sns,water} + Q_{Ltn,water} + Q_{Sns,steam} + Q_{HTE} \quad (A97)$$

Table A1. Thermodynamic properties used to quantify energy demand of electrolysis [39,40].

Component	Δh_f^0 (kJ/mol)	s^0 (kJ/kmolK)	C_p (kJ/kmolK)	C_{Lnt} (kJ/mol)	n
H ₂ (gas)	0	131	$27.28 + 0.00326 T + 50,000/T^2$	-	1
O ₂ (gas)	0	205	$29.96 + 0.00418 T - 167,000/T^2$	-	0.5
HO ₂ (liquid)	-285.83	70	75.44	40.7	1
HO ₂ (gas)	-241.82	189	$30 + 0.01071 T + 33,000/T^2$	-	1

The First Law of thermodynamics is applied to each cooler to determine the heat dissipated by the LP and HP coolers (Equations (A98)–(A100)). Note that the discharge temperature of the HP cooler is preset to the approach temperature plus the ambient temperature ($T_{ac} + T_0$), same as the conventional CAES model. The intake temperature of the high-pressure compressor ($T_{in}^{CM,HP}$) is equal to the exit temperature of the LP cooler. The total compression heat is equal to the heat dissipated in the compressor coolers (Equation (A98)) plus the heat load of the electrolyzer (Equation (A97)), as shown in Equation (A101).

$$Q_{CL} = \int_{P_{em}}^{P_{fl}} (dQ_{CL,LP} + dQ_{CL,HP}) \tag{A98}$$

$$dQ_{CL,LP} = C_p (T_{in}^{CM,HP} - T_{out}^{CM,LP}) dm_{air,ch} \tag{A99}$$

$$dQ_{CL,HP} = C_p (T_{CN,in} - T_{out}^{HTE}) dm_{air,ch} \tag{A100}$$

$$Q_{CM} = Q_{CL} + Q_{HTE, total} \tag{A101}$$

Equations (A19)–(A21) remain valid for quantifying the changes in the internal energy, entropy, and exergy of the compressed air in the cavern. The exergy lost over the charging process of CAES-HTE is calculated by Equation (A102).

$$IX_{ch} = m_{ch} \psi_0 + X_{H2} - \Delta X_{ch} - W_{CM} - W_{HTE} \tag{A102}$$

A.3.3. Roundtrip Performance of CAES-HTE

Equations (A42)–(A46) remain applicable for expressing the roundtrip performance of the CAES-HTE system. Since no fuel is consumed, the heat rate and GHG emissions intensity of HTE-CAES are zero.

The temperature range of the components of the CAES-HTE system in the base case are illustrated in Figure A3.

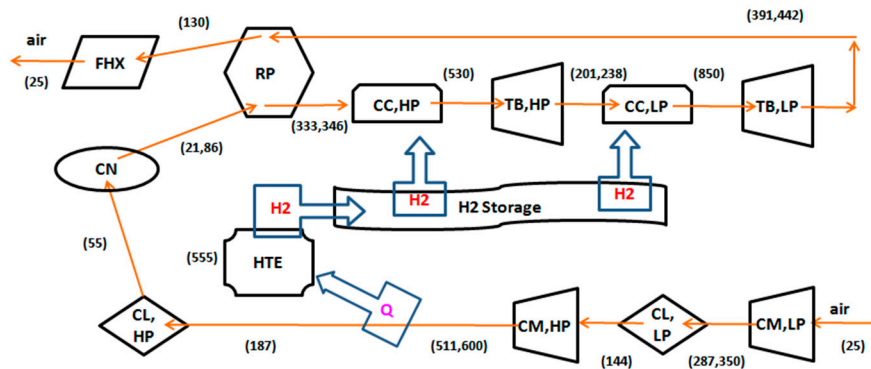


Figure A3. Temperature range of the CAES-HTE system in the base case scenario. Values in each bracket show minimum and maximum temperature. The cavern operates in 5–10 MPa range. The compressor and expander stages have equal pressure ratios.

7. Drury, E.; Denholm, P.; Sioshansi, R. The value of compressed air energy storage in energy and reserve markets. *Energy* **2011**, *36*, 4959–4973. [[CrossRef](#)]
8. Greenblatt, J.B.; Succar, S.; Denkenberger, D.C.; Williams, R.H.; Socolow, R.H. Baseload wind energy: Modeling the competition between gas turbines and compressed air energy storage for supplemental generation. *Energy Policy* **2007**, *35*, 1474–1492. [[CrossRef](#)]
9. Akhil, A.A.; Huff, G.; Currier, A.B.; Kaun, B.C.; Rastler, D.M.; Chen, S.B.; Cotter, A.L.; Bradshaw, D.T.; Gauntlett, W.D. *DOE/EPRI 2013 Electricity Storage Handbook in Collaboration with NRECA*; Sandia National Laboratories: Albuquerque, NM, USA, 2013.
10. Raju, M.; Khaitan, S.K. Modeling and simulation of compressed air storage in caverns: A case study of the Huntorf plant. *Appl. Energy* **2012**, *89*, 474–481. [[CrossRef](#)]
11. Kim, Y.M.; Favrat, D. Energy and exergy analysis of a micro-compressed air energy storage and air cycle heating and cooling system. *Energy* **2009**, *35*, 213–220. [[CrossRef](#)]
12. Buffa, F.; Kemble, S.; Manfrida, G.; Milazzo, A. Exergy and exergoeconomic model of a ground-based CAES plant for peak-load energy production. *Energies* **2013**, *6*, 1050–1067. [[CrossRef](#)]
13. Osterle, J.F. The thermodynamics of compressed air exergy storage. *J. Energy Resour. Technol.* **1991**, *113*, 7–11. [[CrossRef](#)]
14. Skorek, J.; Banasiak, K. Thermodynamic analysis of the compressed-air energy storage systems operation. *Inżynieria Chemiczna i Procesowa* **2006**, *27*, 187–200.
15. Succar, S.; Williams, R.H. *Compressed Air Energy Storage, Theory, Resources, and Applications for Wind Power*; Princeton University: Princeton, NJ, USA, 2008.
16. Zhang, Y.; Yang, K.; Li, X.; Xu, J. The thermodynamic effect of air storage chamber model on advanced adiabatic compressed air energy storage system. *Renew. Energy* **2013**, *57*, 469–478. [[CrossRef](#)]
17. Grazzini, G.; Milazzo, A. Thermodynamic analysis of CAES/TES systems for renewable energy plants. *Renew. Energy* **2008**, *33*, 1998–2006. [[CrossRef](#)]
18. Wolf, D.; Budt, M. LTA-CAES: A low-temperature approach to adiabatic compressed air energy storage. *Appl. Energy* **2014**, *125*, 158–164. [[CrossRef](#)]
19. Hartmann, N.; Vohringer, O.; Kruck, C.; Eltrop, L. Simulation and analysis of different adiabatic compressed air energy storage plant configurations. *Appl. Energy* **2012**, *93*, 541–548. [[CrossRef](#)]
20. Steta, F.D.S. *Modeling of an Advanced Adiabatic Compressed Air Energy Storage (AA-CAES) Unit and an Optimal Model-Based Operation Strategy For Its Integration Into Power Markets*; Swiss Federal Institute of Technology: Zurich, Switzerland, 2010.
21. Arsie, I.; Marano, V.; Nappi, G.; Rizzo, G. A model of a hybrid power plant with wind turbines and compressed air energy storage. In Proceedings of the ASME Power Conference, Chicago, IL, USA, 5–7 April 2005; pp. 987–1000.
22. Bullough, C.; Gatzen, C.; Jakiel, C.; Koller, M.; Nowi, A.; Zunft, S. Advanced adiabatic compressed air energy storage for the integration of wind energy. In Proceedings of the European Wind Energy Conference (EWEC 2004), London, UK, 22–25 November 2004.
23. Khaitan, S.K.; Raju, M. Dynamics of hydrogen powered CAES based gas turbine plant using sodium alanate storage system. *Int. J. Hydrog. Energy* **2012**, *37*, 18904–18914. [[CrossRef](#)]
24. Bidini, G.; Grimaldi, C.N.; Postrioti, L. Thermodynamic analysis of hydraulic air compressor-gas turbine power plants. *Proc. Inst. Mech. Eng. Part A J. Power Energy* **1997**, *211*, 429–437. [[CrossRef](#)]
25. Enis, B.M.; Lieberman, P.; Rubin, I. Operation of hybrid wind-turbine compressed-air system for connection to electric grid networks and cogeneration. *Wind Eng.* **2003**, *27*, 449–459. [[CrossRef](#)]
26. Lund, H.; Salgi, G. The role of compressed air energy storage (CAES) in future sustainable energy systems. *Energy Convers. Manag.* **2009**, *50*, 1172–1179. [[CrossRef](#)]
27. Kim, Y.M.; Lee, J.H.; Kim, S.J.; Favrat, D. Potential and evolution of compressed air energy storage: Energy and exergy analyses. *Entropy* **2012**, *14*, 1501–1521. [[CrossRef](#)]
28. Li, Y.; Wang, X.; Li, D.; Ding, Y. A trigeneration system based on compressed air and thermal energy storage. *Appl. Energy* **2012**, *99*, 316–323. [[CrossRef](#)]
29. Najjar, Y.S.H.; Jubeh, N.M. Comparison of performance of compressed-air energy-storage plant with compressed-air storage with humidification. *Proc. Inst. Mech. Eng. Part A J. Power Energy* **2006**, *220*, 581–588. [[CrossRef](#)]

30. Xia, C.; Zhou, Y.; Zhou, S.; Zhang, P.; Wang, F. A simplified and unified analytical solution for temperature and pressure variations in compressed air energy storage caverns. *Renew. Energy* **2015**, *74*, 718–726. [[CrossRef](#)]
31. Jakiel, C.; Zunft, S.; Nowi, A. Adiabatic compressed air energy storage plants for efficient peak load power supply from wind energy: The European project AA-CAES. *Int. J. Energy Technol. Policy* **2007**, *5*, 296–306. [[CrossRef](#)]
32. Zunft, S.; Jakiel, C.; Koller, M.; Bullough, C. Adiabatic compressed air energy storage for the grid integration of wind power. In Proceedings of the Sixth international workshop on large-scale integration of wind power and transmission networks for offshore windfarms, Delft, The Netherlands, 26–28 October 2006.
33. Weber, O. Huntorf air storage gas turbine power plant. *Brown Boveri Rev.* **1975**, *62*, 332–337.
34. *Compressed Air Energy Storage State-of-Science*; Electric Power Research Institute (EPRI): Palo Alto, CA, USA, 2009.
35. Knoke, S. Compressed air energy storage (CAES). In *Handbook of Energy Storage for Transmission or Distribution Applications*; Eckroad, S., Ed.; The Electric Power Research Institute (EPRI): Palo Alto, CA, USA, 2002.
36. Wright, S. *Reference Design Description and Cost Evaluation for Compressed Air Energy Storage Systems*; Electric Power Research Institute (EPRI): Palo Alto, CA, USA, 2011; p. 104.
37. Gupta, R.B. *Hydrogen Fuel: Production, Transport, and Storage*; CRC Press: Boca Raton, FL, USA, 2009.
38. Boyce, M.P. Principles of operation and performance estimation of centrifugal compressors. In Proceedings of the Twenty-Second Turbomachinery Symposium, Houston, TX, USA, 14–16 September 1993; pp. 161–177.
39. Liu, M.; Bo, Y.; Xu, J.; Jing, C. Thermodynamic analysis of the efficiency of high-temperature steam electrolysis system for hydrogen production. *J. Power Sources* **2008**, *177*, 493–499.
40. Shin, Y.; Park, W.; Chang, J.; Park, J. Evaluation of the high temperature electrolysis of steam to produce hydrogen. *Int. J. Hydrogen Energy* **2007**, *32*, 1486–1491. [[CrossRef](#)]



© 2017 by the authors. Licensee MDPI, Basel, Switzerland. This article is an open access article distributed under the terms and conditions of the Creative Commons Attribution (CC BY) license (<http://creativecommons.org/licenses/by/4.0/>).